CrossMark

# Seeing Double: ASASSN-18bt Exhibits a Two-component Rise in the Early-time *K2* Light Curve

B. J. Shappee[1], T. W.-S. Holoien[2,58], M. R. Drout[2,59,60], K. Auchettl[3,4,5], M. D. Stritzinger[6,7], C. S. Kochanek[3,8], K. Z. Stanek[3,8], E. Shaya[9], G. Narayan[10]

ASAS-SN,

J. S. Brown[8], S. Bose[11], D. Bersier[12], J. Brimacombe[13], Ping Chen[11], Subo Dong[11], S. Holmbo[6], B. Katz[14], J. A. Muñoz[15,16], R. L. Mutel[17], R. S. Post[18], J. L. Prieto[19,20], J. Shields[8], D. Tallon[17], T. A. Thompson[3,8], P. J. Vallely[8], S. Villanueva, Jr.[8]

ATLAS,

L. Denneau[1], H. Flewelling[1], A. N. Heinze[1], K. W. Smith[21], B. Stalder[22], J. L. Tonry[1], H. Weiland[1]

*Kepler*/K2,

T. Barclay[23,24], G. Barentsen[25,26], A. M. Cody[25,26], J. Dotson[25], F. Foerster[27], P. Garnavich[28], M. Gully-Santiago[25,26], C. Hedges[25,26], S. Howell[25], D. Kasen[29,30], S. Margheim[31], R. Mushotzky[9], A. Rest[10,32], B. E. Tucker[33,34,35], A. Villar[36], A. Zenteno[37]

*Kepler* Spacecraft Team,

G. Beerman[38], R. Bjella[38], G. Castillo[38], J. Coughlin[25,39], B. Elsaesser[38], S. Flynn[38], R. Gangopadhyay[38], K. Griest[38], M. Hanley[38], J. Kampmeier[38], R. Kloetzel[38], L. Kohnert[38], C. Labonde[38], R. Larsen[38], K. A. Larson[40], K. M. McCalmont-Everton[40], C. McGinn[38], L. Migliorini[38], J. Moffatt[38], M. Muszynski[38], V. Nystrom[38], D. Osborne[38], M. Packard[38], C. A. Peterson[40], M. Redick[38], L. H. Reedy[38], S. E. Ross[40], B. Spencer[38], K. Steward[38], J. E. Van Cleve[25,39], J. Vinícius de Miranda Cardoso[25,41], T. Weschler[38], A. Wheaton[38]

Pan-STARRS,

and

J. Bulger[1], K. C. Chambers[1], H. A. Flewelling[1], M. E. Huber[1], T. B. Lowe[1], E. A. Magnier[1], A. S. B. Schultz[1], C. Z. Waters[1], M. Willman[1]

PTSS/TNTS,

E. Baron[42,43], Zhihao Chen[44], James M. Derkacy[42], Fang Huang[44,45], Linyi Li[44], Wenxiong Li[44,46], Xue Li[44], Jun Mo[44], Liming Rui[44], Hanna Sai[44], Lifan Wang[47,48,49], Lingzhi Wang[50], Xiaofeng Wang[44], Danfeng Xiang[44], Jicheng Zhang[44], Jujia Zhang[51], Kaicheng Zhang[44,52], Tianmeng Zhang[50], Xinghan Zhang[44], Xulin Zhao[53], P. J. Brown[48,49], J. J. Hermes[54,59], J. Nordin[55], S. Points[37], A. Sódor[56], G. M. Strampelli[32,57], and A. Zenteno[37]

[1] Institute for Astronomy, University of Hawai'i, 2680 Woodlawn Drive, Honolulu, HI 96822, USA; shappee@hawaii.edu
[2] The Observatories of the Carnegie Institution for Science, 813 Santa Barbara St., Pasadena, CA 91101, USA
[3] Center for Cosmology and AstroParticle Physics (CCAPP), The Ohio State University, 191 W. Woodruff Ave., Columbus, OH 43210, USA
[4] Department of Physics, The Ohio State University, 191 W. Woodruff Avenue, Columbus, OH 43210, USA
[5] Dark Cosmology Centre, Niels Bohr Institute, University of Copenhagen, Blegdamsvej 17, DK-2100 Copenhagen, Denmark
[6] Department of Physics and Astronomy, Aarhus University, Ny Munkegade 120, DK-8000 Aarhus C, Denmark
[7] Visiting Astronomer, Institute for Astronomy, University of Hawaii, 2680 Woodlawn Drive, Honolulu, HI 96822, USA
[8] Department of Astronomy, The Ohio State University, 140 West 18th Avenue, Columbus, OH 43210, USA
[9] Astronomy Department, University of Maryland, College Park, MD 20742-2421, USA
[10] Department of Physics and Astronomy, Johns Hopkins University, Baltimore, MD 21218, USA
[11] Kavli Institute for Astronomy and Astrophysics, Peking University, Yi He Yuan Road 5, Hai Dian District, Beijing 100871, People's Republic of China
[12] Astrophysics Research Institute, Liverpool John Moores University, 146 Brownlow Hill, Liverpool L3 5RF, UK
[13] Coral Towers Observatory, Cairns, Queensland 4870, Australia
[14] Department of Particle Physics and Astrophysics, Weizmann Institute of Science, Rehovot 76100, Israel
[15] Departamento de Astronomía y Astrofísica, Universidad de Valencia, E-46100 Burjassot, Valencia, Spain
[16] Observatorio Astronómico, Universidad de Valencia, E-46980 Paterna, Valencia, Spain
[17] Department of Physics and Astronomy, University of Iowa, Iowa City, IA 52242, USA
[18] Post Observatory, Lexington, MA 02421, USA
[19] Núcleo de Astronomía de la Facultad de Ingeniería y Ciencias, Universidad Diego Portales, Av. Ejército 441, Santiago, Chile
[20] Millennium Institute of Astrophysics, Santiago, Chile
[21] Astrophysics Research Centre, School of Mathematics and Physics, Queens University Belfast, Belfast BT7 1NN, UK
[22] LSST, 950 North Cherry Avenue, Tucson, AZ 85719, USA
[23] NASA Goddard Space Flight Center, 8800 Greenbelt Rd, Greenbelt, MD 20771, USA
[24] University of Maryland, Baltimore County, 1000 Hilltop Cir, Baltimore, MD 21250, USA
[25] NASA Ames Research Center, Moffett Field, CA 94035, USA
[26] Bay Area Environmental Research Institute, P.O. Box 25, Moffett Field, CA 94035, USA
[27] Center for Mathematical Modeling, University of Chile, Santiago, Chile
[28] Department of Physics, University of Notre Dame, 225 Nieuwland Science Hall, Notre Dame, IN, 46556-5670, USA
[29] Department of Astronomy, University of California, Berkeley, CA 94720-3411, USA
[30] Lawrence Berkeley National Laboratory, 1 Cyclotron Road, Berkeley, California 94720, USA
[31] Gemini Observatory, La Serena, Chile
[32] Space Telescope Science Institute, 3700 San Martin Drive, Baltimore, MD 21218, USA
[33] The Research School of Astronomy and Astrophysics, Mount Stromlo Observatory, Australian National University, via Cotter Road, Canberra, ACT 2611, Australia

[34] The ARC Centre of Excellence for All-Sky Astrophysics (CAASTRO), Australia

[35] National Centre for the Public Awareness of Science, Australian National University, Canberra, ACT 2601, Australia

[36] Harvard-Smithsonian Center for Astrophysics, 60 Garden Street, Cambridge, MA 02138, USA

[37] Cerro Tololo Inter-American Observatory, Casilla 603, La Serena, Chile

[38] LASP, University of Colorado at Boulder, Boulder, CO 80303, USA

[39] SETI Institute, 189 Bernardo Avenue, Mountain View, CA 94043, USA

[40] Ball Aerospace and Technologies Corp., Boulder, Colorado, 80301, USA

[41] Universidade Federal de Campina Grande, Campina Grande, Brazil

[42] Homer L. Dodge Department of Physics and Astronomy, University of Oklahoma, Norman, OK, USA

[43] Visiting Astronomer at the Department of Physics and Astronomy, Aarhus University, Ny Munkegade 120, DK-8000 Aarhus C, Denmark

[44] Physics Department and Tsinghua Center for Astrophysics (THCA), Tsinghua University, Beijing, 100084, People's Republic of China

[45] Department of Astronomy, School of Physics and Astronomy, Shanghai Jiao Tong University, Shanghai, 200240, People's Republic of China

[46] Las Cumbres Observatory, 6740 Cortona Drive, Suite 102, Goleta, CA 93117-5575, USA

[47] Purple Mountain Observatory, Chinese Academy of Sciences, Nanjing 210034, People's Republic of China

[48] George P. and Cynthia Woods Mitchell Institute for Fundamental Physics and Astronomy, Texas A. & M. University, USA

[49] Department of Physics and Astronomy, Texas A&M University, 4242 TAMU, College Station, TX 77843, USA

[50] National Astronomical Observatory of China, Chinese Academy of Sciences, Beijing, 100012, People's Republic of China

[51] Yunnan Astronomical Observatory of China, Chinese Academy of Sciences, Kunming, 650011, People's Republic of China

[52] Department of Astronomy, University of Texas at Austin, Austin, TX 78712, USA

[53] School of Science, Tianjin University of Technology, Tianjin, 300384, People's Republic of China

[54] Department of Physics and Astronomy, University of North Carolina, Chapel Hill, NC 27599, USA

[55] Institute of Physics, Humboldt-Universität zu Berlin, Newtonstr. 15, D-12489 Berlin, Germany

[56] Konkoly Observatory, MTA CSFK, Konkoly Thege M. ut 15-17, Budapest, 1121, Hungary

[57] University of La Laguna, Calle Padre Herrera, 38200 San Cristobal de La Laguna, Santa Cruz de Tenerife, Spain

## Abstract

On 2018 February 4.41, the All-Sky Automated Survey for SuperNovae (ASAS-SN) discovered ASASSN-18bt in the *K2* Campaign 16 field. With a redshift of $z = 0.01098$ and a peak apparent magnitude of $B_{max} = 14.31$, ASASSN-18bt is the nearest and brightest SNe Ia yet observed by the *Kepler* spacecraft. Here we present the discovery of ASASSN-18bt, the *K2* light curve, and prediscovery data from ASAS-SN and the Asteroid Terrestrial-impact Last Alert System. The *K2* early-time light curve has an unprecedented 30-minute cadence and photometric precision for an SN Ia light curve, and it unambiguously shows a ∼4 day nearly linear phase followed by a steeper rise. Thus, ASASSN-18bt joins a growing list of SNe Ia whose early light curves are not well described by a single power law. We show that a double-power-law model fits the data reasonably well, hinting that two physical processes must be responsible for the observed rise. However, we find that current models of the interaction with a nondegenerate companion predict an abrupt rise and cannot adequately explain the initial, slower linear phase. Instead, we find that existing published models with shallow $^{56}Ni$ are able to span the observed behavior and, with tuning, may be able to reproduce the ASASSN-18bt light curve. Regardless, more theoretical work is needed to satisfactorily model this and other early-time SNe Ia light curves. Finally, we use *Swift* X-ray nondetections to constrain the presence of circumstellar material (CSM) at much larger distances and lower densities than possible with the optical light curve. For a constant-density CSM, these nondetections constrain $\rho < 4.5 \times 10^5$ cm$^{-3}$ at a radius of $4 \times 10^{15}$ cm from the progenitor star. Assuming a wind-like environment, we place mass loss limits of $\dot{M} < 8 \times 10^{-6} M_\odot$ yr$^{-1}$ for $v_w = 100$ km s$^{-1}$, ruling out some symbiotic progenitor systems. This work highlights the power of well-sampled early-time data and the need for immediate multiband, high-cadence follow-up for progress in understanding SNe Ia.

*Key words:* supernovae: individual (ASASSN-18bt, SN 2018oh)

*Supporting material:* machine-readable table

### 1. Introduction

Type Ia supernovae (SNe Ia) are widely thought to result from the thermonuclear explosion of a carbon–oxygen white dwarf (WD; Hoyle & Fowler 1960) in a close binary system. However, the exact physical nature of the progenitor systems of SNe Ia is not known, and two competing classes of models remain. In the single-degenerate (SD) model, the WD accretes material from a nondegenerate companion, eventually triggering a thermonuclear runaway (Whelan & Iben 1973; Nomoto 1982). In the double-degenerate (DD) model, the companion is another WD, and a runaway reaction is triggered

by the merger of the two WDs, caused either by the removal of energy and angular momentum through gravitational radiation (e.g., Tutukov & Yungelson 1979; Iben & Tutukov 1984; Webbink 1984), or by the perturbations of a third (e.g., Thompson 2011; Katz & Dong 2012; Shappee & Thompson 2013; Antognini et al. 2014) or fourth (Pejcha et al. 2013; Fang et al. 2018) body. Searches for observational features that could distinguish between these models have proven difficult, as current simulations based on both the SD (e.g., Kasen et al. 2009) and DD violent merger models (e.g., Pakmor et al. 2012) provide equally accurate models for the observations of SNe Ia around *B*-band maximum light ($t_{Bmax}$).

Several observational tests for the SD model arise from the fact that the companion is struck by the ejecta from the supernova shortly after explosion. First, interaction between the ejecta and the companion modifies the early rise of the light

curve. The observational consequences depend on the viewing angle, with the strongest effect occurring when the companion is along the line of sight between the observer and the SN. At a fixed viewing angle, emission from this shock interaction scales proportionally with the radius of the companion $R_c$, and this allows early-time observations to constrain the properties of the companion (Kasen 2010). Another observational signature comes from the stripping of material from the companion when it is struck by ejecta from the supernova (e.g., Wheeler et al. 1975; Marietta et al. 2000). Hydrodynamic simulations from Pan et al. (2012b) and Liu et al. (2012) showed that approximately 0.1–0.2 $M_\odot$ of solar-metallicity material is expected to be removed from a main-sequence (MS) companion. Lastly, the interaction between the ejecta and the companion is also expected to affect the future properties of the companion (e.g., Podsiadlowski 2003; Pan et al. 2012a; Shappee et al. 2013). Together, these highlight the need for detailed observational studies of SNe Ia at very early and late times to search for these signatures.

In the past decade, almost two dozen SNe Ia have been discovered early and have relatively well-sampled early-time light curves. Surprisingly, Stritzinger et al. (2018) recently showed that there are two distinct populations of early-time behaviors. One population exhibits blue colors that slowly evolve, and the other population shows red colors and evolves more rapidly. The rising parts of SN Ia light curves also show interesting diversity. Empirically, the early light curves of some SNe Ia are reasonably well fit by a single power law function (e.g., Nugent et al. 2011; Bloom et al. 2012; Goobar et al. 2015), and others show a 2−4 day nearly linear rise and then an exponential rise (e.g., Contreras et al. 2018). Finally, many of these well-observed SNe placed limits on masses and radii of a possible companion. These include SN 2009ig ($<6\,M_\odot$; Foley et al. 2012), SN 2011fe ($<0.1$–$0.25\,R_\odot$; Bloom et al. 2012; Goobar et al. 2015), KSN 2011a ($<2\,M_\odot$; Olling et al. 2015), KSN 2011b ($<2\,M_\odot$; Olling et al. 2015), SN 2012cg ($<0.24\,R_\odot$; Silverman et al. 2012; Marion et al. 2016; Shappee et al. 2018), SN 2012fr (Contreras et al. 2018), SN 2013dy ($<0.35\,R_\odot$; Zheng et al. 2013), SN 2013gy ($<4\,R_\odot$; Holmbo et al. 2018), SN 2014J ($\lesssim 0.25$–$4\,R_\odot$; Goobar et al. 2015; Siverd et al. 2015), ASASSN-14lp ($\lesssim 0.34$–$11\,R_\odot$; Shappee et al. 2016), SN 2015F($<1.0\,R_\odot$; Im et al. 2015; Cartier et al. 2017), iPTF16abc (Miller et al. 2018), MUSSES1604D (Jiang et al. 2017), and DLT 17u (SN 2017cbv; Hosseinzadeh et al. 2017).

The *Kepler* spacecraft has also obtained a number of early-time SN light curves (e.g., Olling et al. 2015; Garnavich et al. 2016). Though SNe detected by *Kepler* are rare compared to the numbers found by dedicated transient surveys, *Kepler* light curves can be especially illuminating because of the high 30-minute cadence and photometric stability of the observations. Previously, three SNe Ia have been observed by *Kepler*, providing some of the best early light curve sampling available to date, and none of these light curves show signs of interactions with a stellar companion (Olling et al. 2015).

Here we announce the discovery of the Type Ia SN ASASSN-18bt (SN 2018oh) in UGC 04780, which was monitored by the *K2* mission, and analyze the early evolution of the exquisite *K2* light curve. With a peak apparent magnitude of $B_{max} = 14.31 \pm 0.03$ (Li et al. 2018) and a distance of 47.7 Mpc, it is nearer and brighter than any other supernova detected by *Kepler*. In Section 2, we describe our

discovery and observations of ASASSN-18bt. In Section 3, we analyze the *K2* light curve and find that it is best fit with a double-power-law model, implying that there may be two different timescales important for describing the rise of ASASSN-18bt. In Section 4, we find that the emission in the first few days seen in the *K2* light curve cannot be described using only models of the interaction with an SD companion. In Section 5, we find that the rising light curve also cannot be adequately described using published models that smoothly vary the radioactive $^{56}$Ni distribution in the ejecta, although these models do span the observed behavior of the ASASSN-18bt light curve. In Section 6, we also find that the early-time light curves are also inconsistent with published models for interactions with nearby circumstellar material (CSM). In Section 7, X-ray observations are used to place a limit on the mass loss rates prior to explosion. Finally, a summary of our results and a discussion of the implications for the progenitor system and explosion properties of ASASSN-18bt are presented in Section 8.

This work is part of a number of papers analyzing ASASSN-18bt, with coordinated papers from Dimitriadis et al. (2018) and Li et al. (2018). Li et al. (2018) investigate the near-maximum optical properties of ASASSN-18bt and find $\Delta_{m15} = 0.96 \pm 0.03$ mag, $B_{max} = 14.31 \pm 0.03$ mag, $V_{max} = 14.37 \pm 0.03$ mag, $E(B - V)_{MW} = 0.04$, $E(B - V)_{host} = 0 \pm 0.04$ mag, and $t_{B\,max} = 58162.7 \pm 0.3$ day. Li et al. (2018) also find that the light curve of ASASSN-18bt is consistent with the Milky Way reddening inferred from dust maps alone with no additional host-galaxy reddening. This is supported by the lack of observed Na ID absorption at the host galaxy's recession velocity. Using Fit 6 in Table 9 of Folatelli et al. (2010) and the properties derived from the supernova light curve, we estimate the distance to UGC 04780 to be $d = 49 \pm 3$ Mpc. This distance is consistent with the redshift (47.7 Mpc for $z = 0.01098$ and $H_0 = 69.6$, $\Omega_M = 0.286$, $\Omega_\Lambda = 0.714$; Schneider et al. 1990) and is used throughout this work.

## 2. Discovery and Observations

The All-Sky Automated Survey for SuperNovae (ASAS-SN; Shappee et al. 2014) is an ongoing project to monitor the entire visible sky with rapid cadence with the aim to discover bright and nearby transients with an unbiased search method. To do this, we use units of four 14 cm lenses on a common mount hosted by the Las Cumbres Observatory global telescope network (Brown et al. 2013) at multiple sites around the globe. After expanding our network in 2017, we currently have five units located in Hawaii, Chile, Texas, and South Africa, allowing us to observe the entire sky every ∼20 hr, weather permitting, to a depth of $g \simeq 18.5$ mag. As part of the community effort to support *K2* Campaign 16 (Howell et al. 2014; Borucki 2016), ASAS-SN was monitoring the *K2* field with an increased cadence. The effort to monitor the entire *K2* field of view multiple times per day was continued through Campaign 17 and will be extended to monitor the *TESS* fields four to six times per day.

ASASSN-18bt was discovered at J2000 coordinates of R.A. = $09^h06^m39^s.54$ decl. = $+19°20'17''.77$ in *V*-band images obtained by the ASAS-SN unit "Brutus," located on Haleakala in Hawaii on 2018 February 4.410 UT and was promptly announced to the community (Brown et al. 2018). The *K2* field was monitored by all five ASAS-SN units but, unfortunately, ASASSN-18bt exploded while we were still building reference
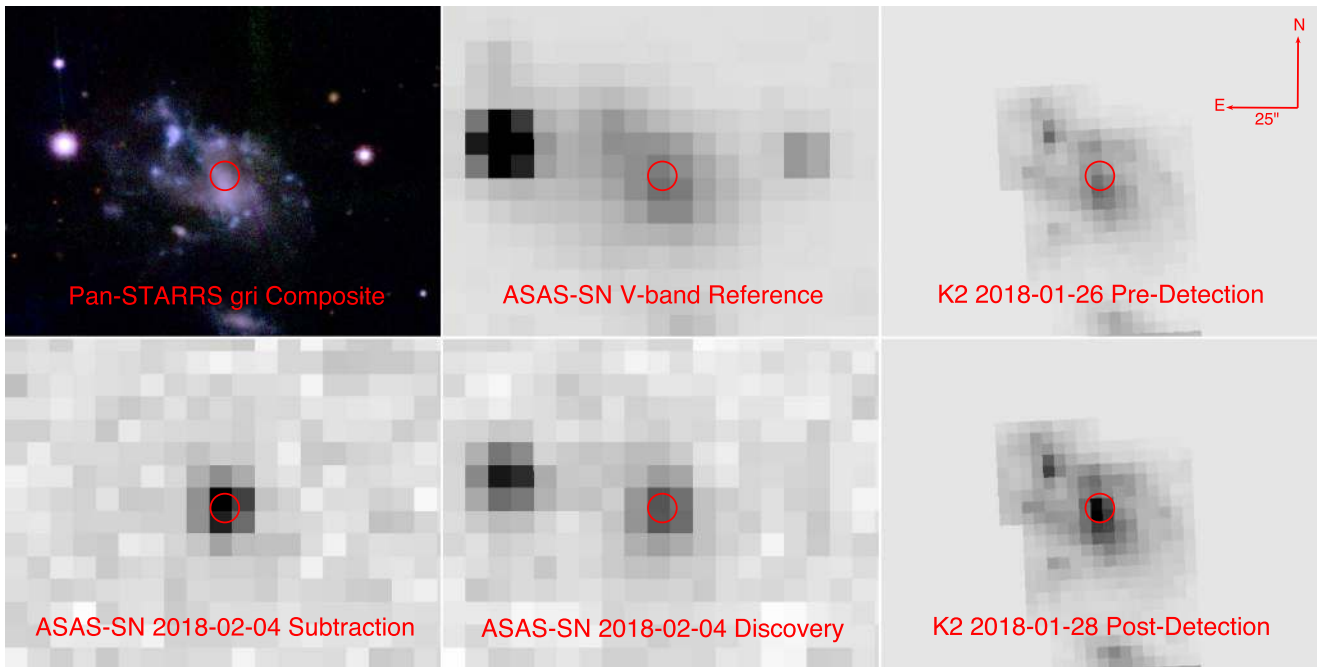
**Figure 1.** Pre- and postdiscovery images of ASASSN-18bt and its host galaxy from Pan-STARRS, ASAS-SN, and *K2*. The top left panel shows a color composite of *g*-, *r*-, and *i*-band images of the host from Pan-STARRS, the top middle panel shows the ASAS-SN *V*-band reference image of the host, and the top-right panel shows a *K2* predetection image obtained on 2018 January 26. The bottom left panel shows the ASAS-SN *V*-band subtraction image from the epoch of discovery, the bottom middle panel shows the ASAS-SN *V*-band discovery image, and the bottom right panel shows a *K2* image from 2018 January 28, after the supernova is visible. The red circle in each image has a radius of $5''.0$ and is centered on the position of the SN. A compass and scale are given in the top right panel for reference.

images on the three recently deployed units, and it was only discovered when a postexplosion image was obtained using an older unit. Worse, the field was not observed between 2018 January 29 and 2018 February 3 because of the field's proximity (within $\sim 30°$) to the moon. If it were not for these factors, ASASSN-18bt would have been discovered substantially earlier. Within 6.8 hr after the discovery, the Asteroid Terrestrial-impact Last Alert System (ATLAS; Tonry et al. 2018) confirmed the source. Almost simultaneously, Leadbeater (2018) spectroscopically classified ASASSN-18bt as an SN Ia based on an $R \sim 150$ spectrum obtained using the modified ALPY spectrograph at Three Hills Observatory.[61] Finally, in Cornect et al. (2018), we gave an improved position of ASASSN-18bt and presented additional photometry obtained by one of our recently deployed ASAS-SN *g*-band units. The analysis of the *K2* light curve had to wait until the end of Campaign 16, 2018 February 25, when the data were downloaded from the *Kepler* spacecraft and became available.

Figure 1 shows the reference image, the 2018 February 4 discovery image, and the 2018 February 4 first detection difference image from the ASAS-SN ba camera in the top middle, bottom middle, and bottom left panels of the figure, respectively. The 2018 January 26 predetection and 2018 January 28 postdetection images of the supernova and its host from *K2* are shown in the top right and bottom right panels of the figure, and the top left panel shows a *gri*-band composite color image of the host galaxy constructed with images obtained by the Panoramic Survey Telescope & Rapid Response System (Pan-STARRS; Chambers et al. 2016; Flewelling et al. 2016). The discovery difference image from

ASAS-SN shows that the supernova is clearly detected and the host flux and flux from nearby stars are cleanly subtracted.

The host galaxy of ASASSN-18bt is UGC 04780 ($z = 0.01098$, Schneider et al. 1990), a blue barred spiral galaxy with blue clumps in its arms, indicating the likely presence of ongoing star formation. Using archival photometry from Pan-STARRS (optical), the *Galaxy Evolution Explorer* (ultraviolet), and the *Wide-field Infrared Explorer* (near-infrared), we fit the spectral energy distribution of UGC 04780 with the publicly available Fitting and Assessment of Synthetic Templates (FAST; Kriek et al. 2009). Given the clumpy nature of the light distribution, we measure the optical magnitudes from the PS1 images by hand and find $g \sim 14.9$ mag, $r \sim 14.5$ mag, $i \sim 14.5$ mag, $z \sim 14.4$ mag, and $y \sim 14.3$ mag. We assumed a Cardelli et al. (1989) extinction law with $R_V = 3.1$ and a Galactic extinction of $A_V = 0.124$ mag (Schlafly & Finkbeiner 2011) and employed an exponentially declining star-formation history, a Salpeter initial mass function, and the Bruzual & Charlot (2003) stellar population models. Based on the FAST fit, the host galaxy has a stellar mass of $(4.68^{+0.33}_{-0.61}) \times 10^8 \, M_\odot$ and a star formation rate of $\lesssim 0.05 \, M_\odot \, \mathrm{yr}^{-1}$, which is largely consistent with the results from the MPA-JHU Galspec pipeline. However, the galaxy light is dominated by a young stellar population, and the modeling has difficulty fitting both the optical and infrared data, suggesting that our mass estimate should be regarded as an upper limit.

## 2.1. ASAS-SN Light Curve

ASAS-SN images are processed by the fully automatic ASAS-SN pipeline using the ISIS image subtraction package (Alard & Lupton 1998; Alard 2000). A host-galaxy reference image was constructed for each of the ASAS-SN units using

---

[61] As described here: http://www.threehillsobservatory.co.uk/astro/spectroscopy.htm.

**Table 1**
Photometric Observations

| JD (−2,450,000) | Band | Magnitude | Telescope |
|---|---|---|---|
| 8105.761 | $g$ | >18.69 | ASAS-SN/bi |
| 7908.470 | $V$ | >17.57 | ASAS-SN/be |
| 8095.490 | $K2$ | >21.12 | K2 |
| 8148.053 | $o$ | 17.126(0.028) | ATLAS |

**Note.** $V$-band photometry is calibrated in the Vega magnitude system. The *Kepler* and SDSS $g$-band photometry is calibrated in the AB magnitude system. Only the first observation in each band is shown here to demonstrate its form and content. The table is included in its entirety as an ancillary file.

(This table is available in its entirety in machine-readable form.)

images obtained prior to the discovery of ASASSN-18bt, and these were used to subtract the host's background in all science images. Science images that were obviously affected by clouds were removed. We then performed aperture photometry with a 2 pixel (≈16″0) aperture on each host-template subtracted science image using the IRAF `apphot` package. Photometry of the supernova was calibrated relative to a number of stars in the field of the host galaxy with known magnitudes from the AAVSO Photometric All-Sky Survey (APASS; Henden et al. 2015). The ASAS-SN detections and $3\sigma$ limits are presented in Table 1 and plotted in Figure 2. Throughout the paper, light curves are plotted in observed time, and measured rise times are translated to the rest frame.

### 2.2. K2 Light Curve

The *K2* mission is a follow-up to the highly successful *Kepler* mission. *K2* was instigated when a second reaction wheel was lost, leaving the spacecraft with only two wheels rather than the three required for full 3D stabilization. The best solution for mitigating this problem was to constrain the spacecraft to point in the ecliptic plane, balancing solar wind pressure about the center of mass and minimizing the torques on the spacecraft that rotate the field around the line-of-sight axis. Thrusters are used every few hours to return the pointing back to a starting orientation, resulting in a sawtooth motion in the positions of stars that is typically on the order of one pixel. This sawtooth pattern is reflected in the photometric counts, but can be reduced by summing over more pixels in a larger aperture, at the cost of introducing more photon noise and contamination from neighboring sources. *K2* also has long-term (weeks and months) sensitivity trends partly due to temperature changes as the Sun angle and zodiacal light levels change within a campaign. *Kepler* and *K2* have a broad response function over ~420–900 nm (Koch et al. 2010).

When *K2* Campaign 16 ended, all data for the campaign were downloaded from the spacecraft. The unique nature of the *K2* mission requires careful reduction. Unfortunately, the relevant CCD channel had moving bands of an electronic pattern called rolling bands during the observation. This is a not-uncommon occurrence on *K2*, and there are flags in the quality arrays that indicate when it passes over the optimal aperture for a target. Because the pattern is fairly constant along a row, we were able to minimize its effects by subtracting the mean at the edges of the downloaded target pixel map (after ignoring pixels that appear to have galaxy or starlight). From examining other galaxies in the channel with this problem, we

find that this noise is usually reduced to a level below the shot noise of the background light. The data taken when the rolling bands were present in the ASASSN-18bt aperture were mostly constrained within 3 days of $t_1$ (as fit in Section 3). To remove the sawtooth pattern created by changes in the amount of light overfilling the aperture, as *K2* nods because of solar wind pressure, third-order polynomials in two dimensions of centroidal motion were fit to all galaxies observed on the same channel, except for those clearly undergoing variability. To remove longer timescale trends, we obtain basis vectors from a principle component analysis (PCA) of these light curves. The light curves on this channel can then be approximated as a linear superposition of these vectors plus a unique sawtooth pattern for each galaxy. However, the solutions for the sawtooth patterns remain poor as long as the trending vectors are poor, and vice versa. Therefore, an iterative scheme is applied in which we put the long-term trends back into the light curves, rerun the PCA analysis, and solve for improved basis vectors. Then, after solving for the coefficients of both the sawtooth fit and the trending vectors again, we repeat the procedure. After about a dozen iterations, the procedure converges for the most common five trending vectors.

The coefficients to apply to the trending vectors are found by minimizing the variation of the light curve after dividing by the linear superposition of the PCA vectors. This works well because most galaxies have a constant brightness over the campaign. But for a galaxy with a transient like ASASSN-18bt, we are confined to using only the part of the light curve with quiet time before or after the event. Fortunately, the optimal number of PCA vectors for ASASSN-18bt was just two, and there was a long period in the campaign before eruption to use to determine their coefficients well.

An additional complication is created because an SN moves the center of light from the center of the galaxy toward the SN. This induces a slight change in the sawtooth function. Therefore, after solving for the best sawtooth and long-term instrumental trending during the quiet time, the sawtooth pattern is removed from the time when the SN exceeds 50% of the galaxy contribution, and a new sawtooth pattern is obtained. This time, the trending is assumed to be valid, and the goodness of fit is a measure of how well the corrected light curve fits the pattern after smoothing over three or four nodding periods.

Finally, we calibrated the *K2* light curve using the mangled SED from fitting the PS $r$-band (presented in Li et al. 2018) around the peak to determine the synthetic *K2* peak magnitude and the absolute zero point to the *K2* light curve. The *K2* detections and $3\sigma$ limits are shown in Figure 2 and, for completeness, presented in Table 1.

### 2.3. ATLAS Light Curve

ATLAS is an ongoing survey project primarily designed to detect small (10–140 m) asteroids that are on a collision course with Earth. ATLAS scans the entire sky accessible from Hawaii every few days using fully robotic 0.5 m $f/2$ Wright Schmidt telescopes located on the summit of Haleakalā and at Mauna Loa Observatory. Each telescope has a 5°.4 × 5°.4 field of view with 1″.86 pixels, and during normal operations each telescope obtains four 30 s exposures of 200–250 target fields per night. This allows the two telescopes together to cover roughly half of the accessible sky per night, with the four observations of a given field typically obtained within less than an hour. The
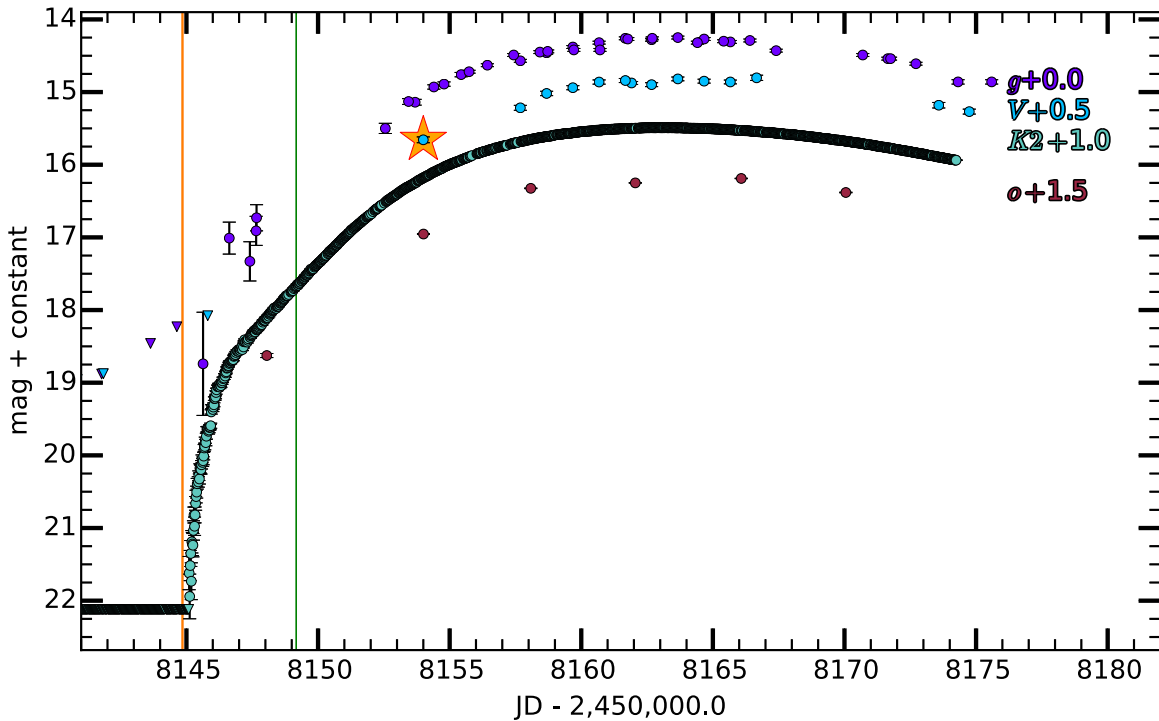
**Figure 2.** Host-subtracted light curves of ASASSN-18bt from ASAS-SN (*V* and *g* filters), *K2* (*Kepler* filter), and ATLAS ("orange" or *o* filter). Here, $3\sigma$ limits are shown as downward triangles for epochs where the supernova was not detected. The orange and green vertical bars indicate $t_1$ and $t_2$, respectively, as determined by a double-power-law fit to the *K2* light curve (see Section 3 and Equation (1)). The orange star highlights the ASAS-SN discovery epoch of ASASSN-18bt.

ATLAS telescopes use two broad filters: the "cyan" filter (*c*) covering 420–650 nm and the "orange" filter (*o*) covering 560–820 nm (Magnier et al. 2016; Tonry et al. 2018).

Every image from the ATLAS telescopes is processed by a fully automated pipeline that performs flat-fielding, astrometric calibration, and photometric calibration. A low-noise reference image constructed by stacking multiple images of the appropriate field taken under excellent conditions is then subtracted from each new image, allowing the detection and discovery of asteroids and other transient sources.

We performed forced photometry on the subtracted ATLAS images of ASASSN-18bt as described in Tonry et al. (2018). We then took a weighted average of the intranight photometric observations to get a single flux measurement for each night of observation. The ATLAS photometry and $3\sigma$ limits are presented in Table 1 and are shown in Figure 2.

## 3. Characterizing the Early Light Curve

The high cadence and photometric precision of *Kepler* give us an extremely well-sampled early light curve, allowing us to fit and model the physical parameters of the supernova with a high degree of accuracy. To get a more realistic estimate for the point-to-point errors, we measure the mean and standard deviation in the *K2* light curve from the beginning of Campaign 16 until 5 days before there is any signature of ASASSN-18bt in the light curve. We take that to be the point-to-point error for the entire *K2* light curve. This method cannot account for any systematic errors that are coherent in time.

As seen in the left panel of Figure 3, it is obvious that a single power law with an arbitrary power-law index ($\alpha$) cannot adequately describe the light curve. This also rules out an expanding fireball model where flux is proportional to a specific, $(t - t_1)^2$, power law (Arnett 1982). Thus, ASASSN-18bt joins a

growing sample of SNe Ia with some structure in their early light curves that cannot be described by a single-power-law model. It is interesting to ask what causes this structure, but first it must be characterized.

To do so, we fit the *K2* light curve with a double power law of the form

$$
\begin{aligned}
f &= z \quad \text{when } t < t_1, \\
f &= z + h_1(t - t_1)^{\alpha_1} \quad \text{when } t_1 \leqslant t < t_2, \\
f &= z + h_1(t - t_1)^{\alpha_1} + h_2(t - t_2)^{\alpha_2} \quad \text{when } t_2 \leqslant t,
\end{aligned}
\tag{1}
$$

using the `emcee` Markov chain Monte Carlo package (Foreman-Mackey et al. 2013). Figure 3 shows the *K2* light curve and the best-fitting double-power-law model (top panel), as well as the fit residuals (bottom panel). The double power law describes the rising *K2* light curve well with just seven free parameters. The pattern in the residuals is likely not due to the sawtooth thruster firing described in Section 2.2 because the residuals are mostly symmetric in time and occur over too long of a period. Thus, the residuals likely indicate that there is some behavior not completely captured by our double-power-law model. However, the reasonable fit and two different timescales in Equation (1) imply that there may be two different physical processes contributing to the light curve. We will explore potential physical models in the next few sections.

To estimate the peak flux and the time of maximum in the *Kepler* bandpass, we fit a quadratic function to the *K2* light curve within 2 days of the peak. This allows us to scale the light curve shown in Figure 3 to the peak and to compute the rise time in the *K2* filter alone, which is important when comparing to the previous SNe Ia observed by *Kepler*. From the double-power-law fit, we find that $t_1 = 2458144.850^{+0.001}_{-0.001}$, and with the quadratic fit to the peak, we find a rise time of
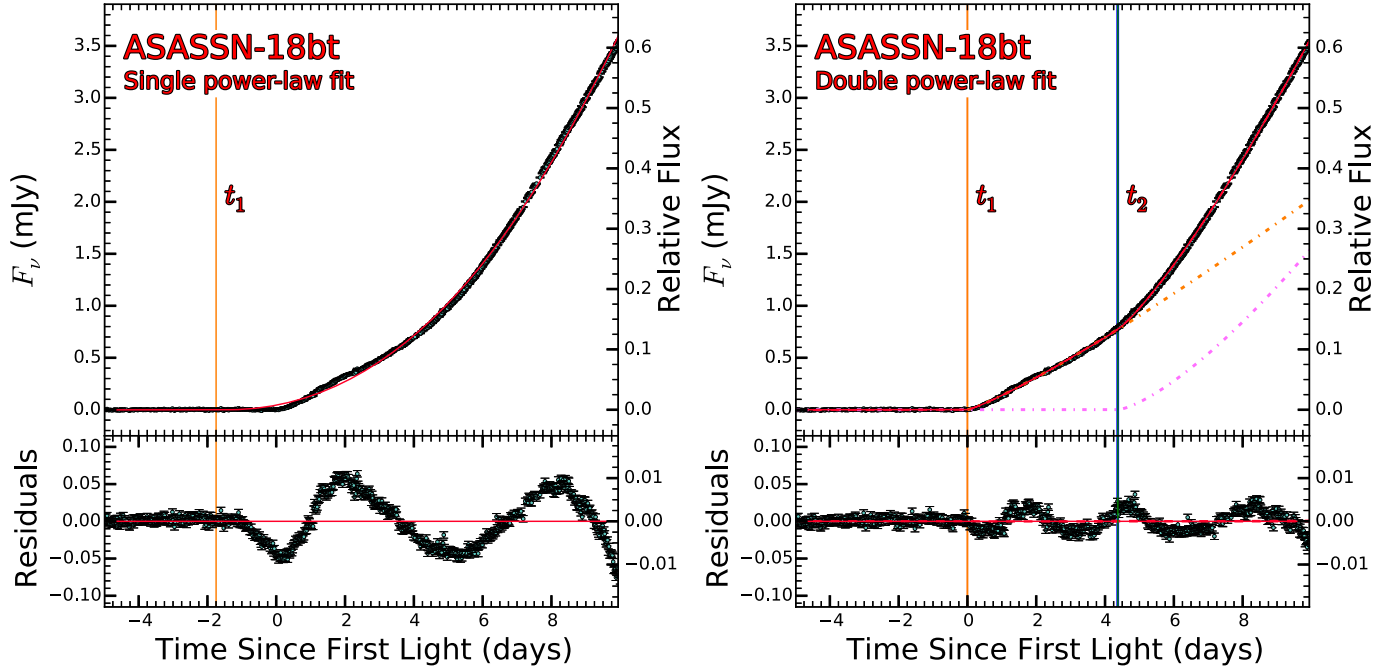
**Figure 3.** The *K2* early-time light curve of ASASSN-18bt and the corresponding best-fit single-power-law (left panel) and double-power-law models (right panel). Top: *K2* flux relative to maximum brightness. The red line shows the best fit of Equation (1) to the *K2* light curve. The red dashed lines indicate the $1\sigma$ error on the fit but are mostly underneath the solid red line. The orange and pink dot-dashed lines show the two components of the fit. Bottom: residuals from the models. The vertical orange and green lines indicate $t_1$ and $t_2$, respectively.

$t_{\rm rise} = t_{\rm peak} - t_1 = 18.125^{+0.008}_{-0.008}$ days. Throughout this work, we use this best-fit estimate of $t_1$ as the temporal origin.

We also fit the previous three SNe Ia observed by *Kepler* (Olling et al. 2015) with the same double- and single-power-law models. Figure 4 shows these light curves and their corresponding best fits. In order to facilitate comparison among the four *Kepler* SNe Ia, Figure 4 uses the same scale as Figure 3. The best-fit parameters from Equation (1) are shown for all four SNe in Table 2. In the table, $t_{\rm rise}$ is the time from $t_1$ to the maximum in the *K2* filter ($t_{\rm peak}$), while $t_{B\rm rise}$ is the time from $t_1$ to the estimated time of *B*-band maximum light. All three objects can be nearly equally well described by either a single- or double-power-law fit, and there is no compelling evidence that KSN 2011b, KSN 2011c, or KSN 2012a light curves require the second power-law component. However, the light curves of all three SNe are substantially noisier, which would mask early-time behaviors. To demonstrate this, we determine the earliest time ($t_{\rm det}$) the SN light curve is $1\sigma$ above the average preexplosion flux. Of the four *Kepler* SNe, only ASASSN-18bt is confidently detected within the first day of $t_1$.

Next we explore some of the physical processes that could be responsible for the double-power-law structure in the early light curve of ASASSN-18bt.

## 4. Early-time Light Curve and Companion Constraints

If the progenitor of an SN Ia is a WD accreting from a nondegenerate companion, then its ejecta are expected to interact with the companion after explosion, potentially producing an imprint on the early, rising light curve. The strength of this signature is thought to depend on the viewing angle with respect to the progenitor system, with the strongest effect occurring when the companion lies along the line of sight between the observer and the supernova. The effect scales

proportionally with the radius of the companion, $R_c$, when the viewing angle is fixed. In this section, we compare the early rise of ASASSN-18bt with emission models derived for the interaction between SN Ia ejecta and different sizes of companions, in order to investigate whether interaction with a companion can explain the double-power-law structure in the light curve and to place limits on $R_c$. We used the analytic models from Kasen (2010) to generate light curves for a variety of $R_c$ assuming the companion is aligned with our line of sight, where the signature is expected to be largest. We also assumed that the companion was Roche-lobe overflowing and that the masses of the primary and companion are 1.4 and 1.0 $M_\odot$, respectively. This introduces a weak dependency on mass (Eggleton 1983), but the mass dependence is unimportant compared to the unknown viewing angle.

First we simply compared the Kasen (2010) models to our early-time data assuming that the time of explosion ($t_{\rm exp}$) was the same as the $t_1$ measured from the double-power-law fit in Section 3. While $t_{\rm exp}$ and $t_1$ have occasionally been used interchangeably, they need not be the same because there is a possible dark phase between the explosion and when the supernova first starts to brighten (Hachinger et al. 2013; Piro & Nakar 2014; Piro & Morozova 2016). Piro & Morozova (2016) showed that even in extreme cases, dark phases last <2 days, and more realistically last $\lesssim$1 day. This effect will be discussed more in Section 5.

In the top row of Figure 5, we compare the early light curves from *K2*, ASAS-SN, and ATLAS to the interaction models for a 0.1, 1.0, 10.0, and 40.0 $R_\odot$ companion. In the upper left panel, it can be immediately seen that if the initial nearly linear rise is to be explained by the interaction with a companion, it must be a large companion ($\sim$40 $R_\odot$) to produce a large enough signature. However, the upper center and upper right panels show that the early *K2*, ASAS-SN *g*-band, and ASAS-SN
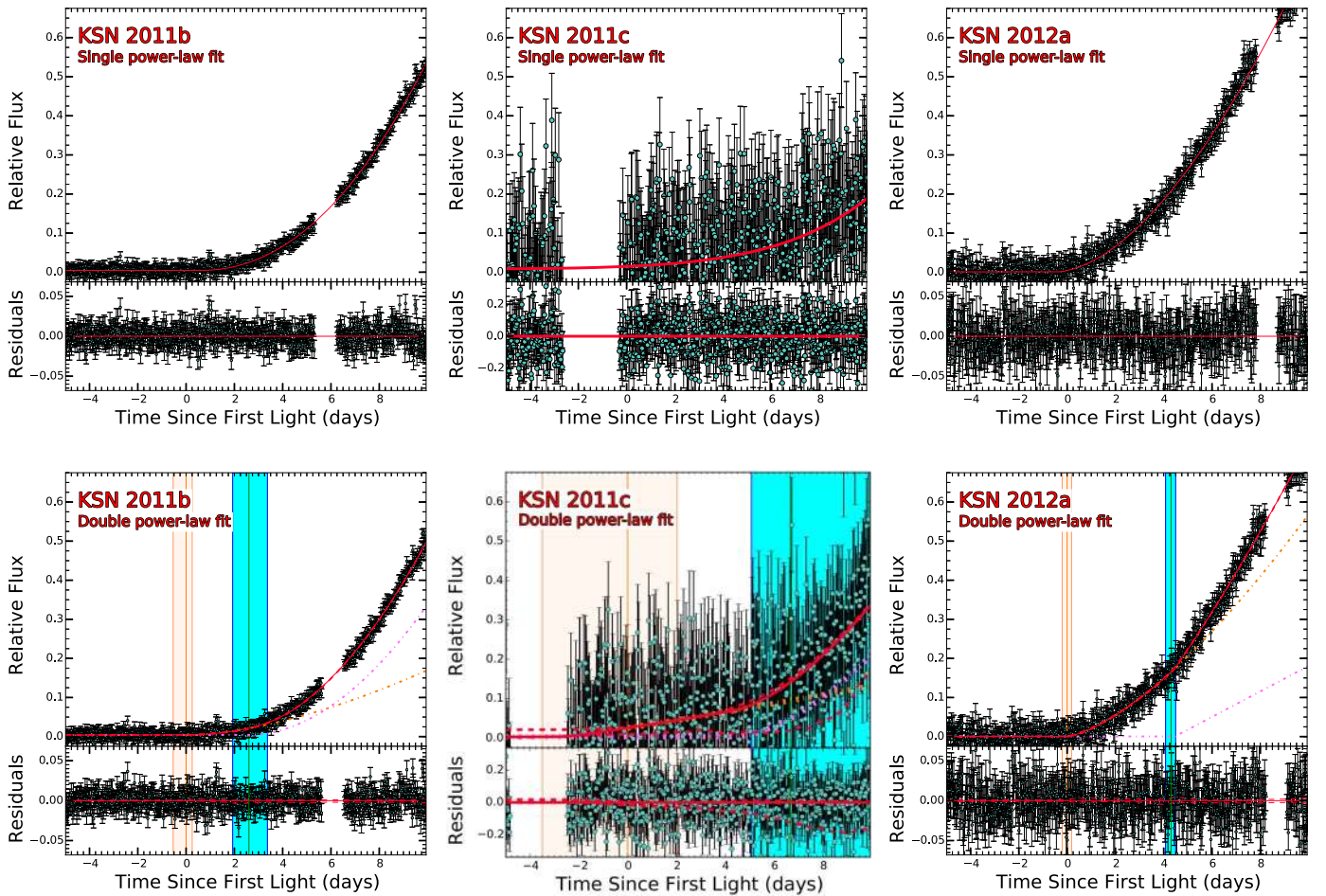
**Figure 4.** *Kepler* light curves and best-fit single- (upper row) and double-power-law models (bottom row) for the other three SNe Ia observed with *Kepler* (Olling et al. 2015). Colors have the same meanings as in Figure 3, and the supernova names are given in the top left corner of each panel. The light curves are plotted on the same scale as in Figure 3 to enable comparison between the four SNe, while the residual panels are individually scaled for each supernova to enable a comparison of the quality of the fits. The second power law is not constrained for KSN 2011c because of the noisier data.

*V*-band light curves are inconsistent with such a large signature from a companion, and we immediately rule out companions significantly larger than ∼10 $R_\odot$ for our assumed viewing angle.

To further demonstrate that the early-time light curve of ASASSN-18bt cannot be described by a single-power-law rise combined with an interaction with a companion, we construct a grid of companion models and simultaneously fit the companion radius and power-law component. The best-fit model is shown in the bottom left panel of Figure 5. The best-fit companion radius is 25 $R_\odot$, but the fit has large residuals. The main issue is that the interactions produce a light curve that rises rapidly and then flattens, while the observed light curve rises nearly linearly and then steepens (see Table 2). As discussed in the previous paragraph, such a large companion is also inconsistent with the bluer ASAS-SN prediscovery data. Thus, if an interaction with a companion contributes significantly to the rise of ASASSN-18bt, the intrinsic rise of the SN itself must be more complicated than a single power law.

Next we simultaneously fit for a companion radius and a double-power-law model (Equation (1)). We constrained the dark time to ($t_1 - t_{exp}$) to be positive, assuming the progenitor cannot emit significant flux prior to explosion, and less than 2.0 days. Additionally, we constrained $h_1$ and $h_2$ to be positive and

$a_1$ and $a_2$ to be greater than 1. Finally, we constrained $t_1$ to be within 0.3 days of $t_{det}$ as measured in Section 3.

We find that the first power-law component and the companion can compensate for each other and that the dark time, the power-law index, and the companion radius are degenerate because the Kasen (2010) companion models initially rise quickly and then turn over in the *K2* filter, whereas any power law with $\alpha_1 > 1$ does the opposite. Thus a nearly linear rise is possible in the first ∼4 days without any strong kinks or features. This, however, requires fine-tuning of the power law and companion to hide the shock signature in a smooth curve, although, strictly speaking, solutions can be found.

To place a statistical limit on the radius of a companion assuming the rise can be well described by a double-power-law model, we first found the best fit for companion models from 0.01 to 50.0 $R_\odot$. We found nearly identically good fits for radii from 0.01 to 8 $R_\odot$ before the fits begin to deteriorate. To place a statistical upper limit, we focus between −0.5 and 2 days, where a companion might contribute significantly to the light curve. We then found where the $\chi^2$ probability distribution was <0.32 and <0.05 during that time period. We find that the largest radii of companions that have acceptable fits under these criteria are 8.0 $R_\odot$ and 11.5 $R_\odot$, respectively. For reference, we plot the smallest companion radius ruled out at $1\sigma$ in the

**Table 2**
Photometric Observations

| SN | $t_1$ (JD) | $t_2 - t_1$ (days) | $\alpha_1$ | $\alpha_2$ | $t_{\rm rise}$ (days) | $t_{B\rm rise}$ (days) | $t_{\rm det} - t_1$ (hr) |
|---|---|---|---|---|---|---|---|
| ASASSN-18bt | $2458144.850^{+0.001}_{-0.001}$ | $4.373^{+0.020}_{-0.016}$ | $1.167^{+0.004}_{-0.003}$ | $1.393^{+0.005}_{-0.007}$ | $18.125^{+0.008}_{-0.008}$ | $18.150^{+0.297}_{-0.297}$ | $1.438^{+0.027}_{-0.000}$ |
| KSN 2011b | $2455827.6^{+0.6}_{-0.3}$ | $2.6^{+0.6}_{-1.1}$ | $1.9^{+0.7}_{-0.4}$ | $1.9^{+0.2}_{-0.1}$ | $18.7^{+0.4}_{-0.6}$ | $18.3^{+0.6}_{-0.8}$ | $55^{+17}_{-6}$ |
| KSN 2011c | $2455907.4^{+2.1}_{-1.2}$ | $\cdots$ | $2.2^{+1.1}_{-0.4}$ | $\cdots$ | $19.1^{+1.1}_{-1.8}$ | $18.8^{+1.1}_{-1.8}$ | $131^{+71}_{-6}$ |
| KSN 2012a | $2456161.1^{+0.2}_{-0.2}$ | $4.3^{+0.3}_{-0.3}$ | $1.4^{+0.1}_{-0.1}$ | $1.07^{+0.05}_{-0.08}$ | $15.1^{+0.3}_{-0.3}$ | $14.8^{+0.5}_{-0.5}$ | $22^{+20}_{-2}$ |

**Note.** Fit parameters of the double-power-law model (Equation (1)) for the four SNe Ia observed with *Kepler* to date. A second power law is not constrained for KSN 2011c, likely because its light curve is significantly noisier, due to its greater distance.

bottom center and bottom right panels of Figure 5. It can be seen that to fit a $9\,R_\odot$ companion, $t_{\rm exp}$ is being pushed to be later than in the fits using only a double power law and that the model misses the earliest rise of the light curve. This weak constraint on the progenitor system demonstrates that a physically motivated model for the rising SN light curve is required before we can confidently use early-time light curves of SNe Ia to constrain their progenitor systems.

## 5. Comparison to $^{56}$Ni Mixing Models

Very early-time emission from SNe Ia can probe the location of $^{56}$Ni in the ejecta (e.g., Piro & Nakar 2013) and thus can be used as a diagnostic of the explosion physics. In Piro & Morozova (2016), the authors used the open-source SuperNova Explosion Code (SNEC; Morozova et al. 2015) to investigate how the distribution of $^{56}$Ni can affect the earliest phases of SN Ia light curves. Models with $^{56}$Ni significantly mixed into the ejecta result in a quicker rise than those with $^{56}$Ni more centrally concentrated. Contreras et al. (2018) matched the early light curve of SN 2012fr with model light curves predicted for different levels of $^{56}$Ni mixing. They found that the early steepening seen in the light curve of SN 2012fr could be accounted for by a model with a $^{56}$Ni mass fraction of 0.05 at approximately $0.05\,M_\odot$ below the surface of the WD.

We used the same $^{56}$Ni mixing models as Contreras et al. (2018). However, even after appropriately rescaling the models for Milky Way reddening, host galaxy reddening, and differences in distance, we still found that the Contreras et al. (2018) models underpredicted the observed *K2* light curve. We assume that this difference is due to the modest difference in passbands between the LSQ *gr*-band used to construct the models and the *K2* bandpass, along with differences in the total $^{56}$Ni production between the two SNe. We found that scaling the models by 130% brought them into reasonable agreement with the *K2* data.

In Figure 6 (left panel), we show the scaled ($\sim$60%) $^{56}$Ni mixing models from Contreras et al. (2018), using the same colors and scales, along with the *K2* light curve of ASASSN-18bt. The right panel shows the corresponding $^{56}$Ni distributions for each model. The very early light curve is most consistent with a model where the $^{56}$Ni is significantly mixed, with a $^{56}$Ni mass fraction of 0.15–0.2 at approximately $0.05\,M_\odot$ below the surface of the WD. However, $\sim$3 days after first light, the light curve becomes more consistent with the moderately mixed $^{56}$Ni curves, similar to SN 2012fr. This might imply that the $^{56}$Ni distribution in the ejecta is not smoothly varying or monotonically decreasing with radius in ASASSN-18bt.

Finally, in the left panel of Figure 7, we compare the *K2* light curve to synthetic light curves from Noebauer et al. (2017), who used the radiation hydrodynamical code Stella to compute light curves for a variety of explosion models. We compare ASASSN-18bt to the scaled, predicted *V*-band light curves for four explosion models:

(1) The parameterized 1D ejecta structure of the W7 model of Nomoto et al. (1984).
(2) The centrally ignited detonation of a sub-Chandrasekhar mass CO WD (SubChDet; Sim et al. 2010).
(3) A "double-detonation" model where an initial detonation in an accreted He surface layer triggers carbon detonation in the core of the sub-Chandrasekhar mass WD (SubChDoubleDet; Fink et al. 2010; Kromer et al. 2010).
(4) The "violent merger" of two sub-Chandrasekhar mass CO WDs, which triggers the more massive to detonate (Merger; Pakmor et al. 2012).

As seen in Figure 7, only the double-detonation model can qualitatively match the rise for the first few days. In this model, He burning leaves radioactive isotopes near the surface of the ejecta, similar to the $^{56}$Ni mixing models. Lastly, collision models (e.g., Dong et al. 2015, 2018) may also produce similar features, but the early-time light curves from this model have not, to the authors' knowledge, been investigated thoroughly.

## 6. Interaction with Nearby CSM

The presence of a dense CSM can also affect the early-time rising light curve. As previously discussed, some SNe Ia models have nearby nondegenerate companions, but more general distributions of material are possible. Most progenitor scenarios require mass transfer, which is not a completely efficient process. Piro & Morozova (2016) investigated the possible impact of this material on the early-time light curves of SNe Ia. Motivated by the postmerger studies of Pakmor et al. (2012), Shen et al. (2012), and Schwab et al. (2012), Piro & Morozova (2016) argue that the nearby CSM is likely distributed as $\rho \propto r^{-3}$ and model the resulting light curves as a function of the total circumstellar mass ($M_e$) and its outer radius ($R_e$). They also explore different $^{56}$Ni distributions implemented as a boxcar average with width $S$ in mass.

In the right panel of Figure 7, we compare the Piro & Morozova (2016) models to the *K2* light curve of ASASSN-18bt. Piro & Morozova (2016) presented model *V*-band light curves, whereas the *K2* filter is significantly broader. We fit each model to ASASSN-18bt, varying $t_{\rm exp}$ and the flux scaling. While filter differences may lead to some systematic uncertainties, we can qualitatively see that none of these models
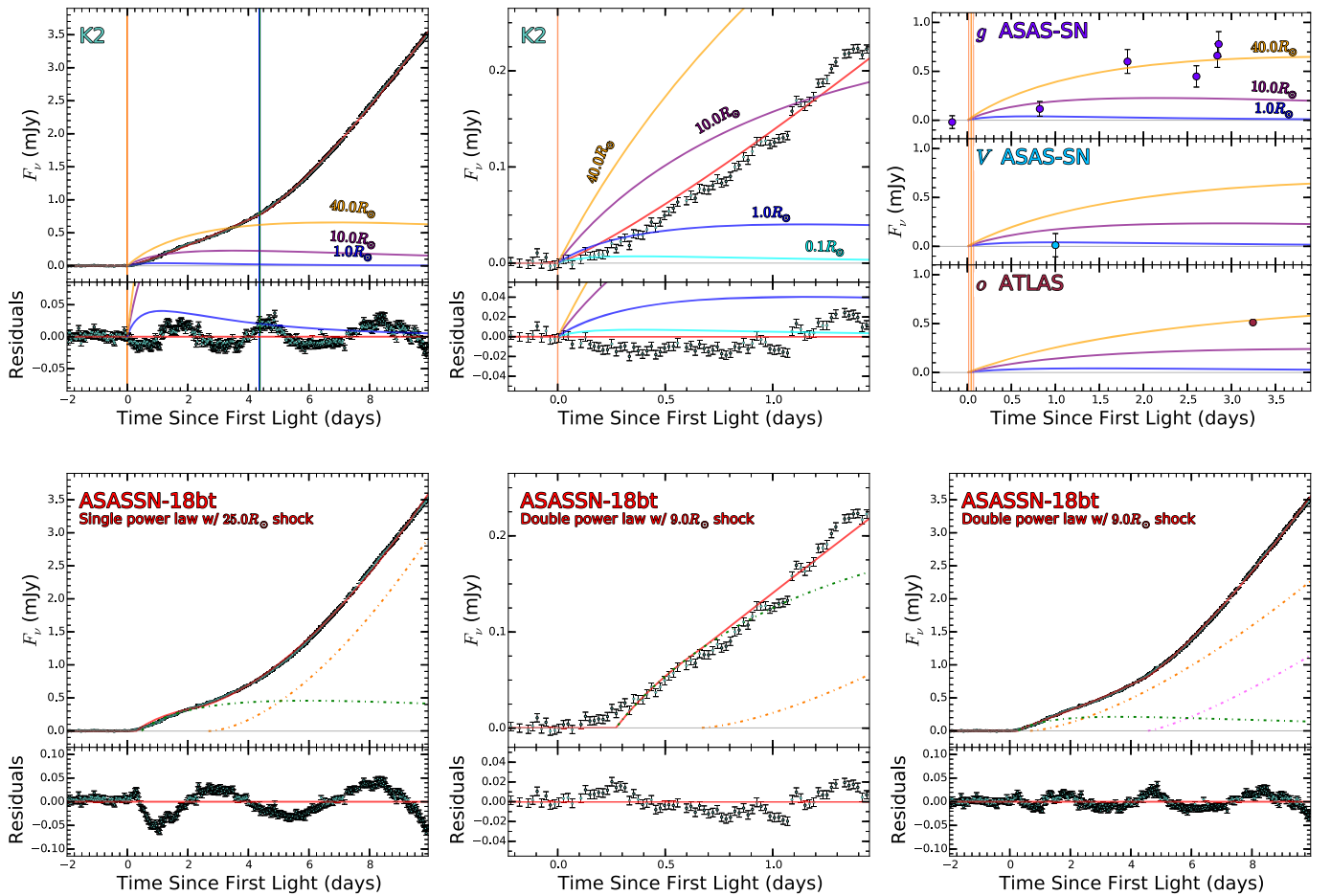
**Figure 5.** Top row: *K2*, ASAS-SN, and ATLAS light curves of ASASSN-18bt compared to the Kasen (2010) models of emission from the interaction of the supernova shock with companions of various radii assuming the companion is along our line of sight. The left and center panels show the first 10 and 1.5 days following $t_1$. The right panel shows the ASAS-SN and ATLAS light curves. Bottom row: The left panel shows the *K2* light curve fit with a best-fit single-power-law and companion model. It can be seen that a single-power-law and companion model cannot satisfactorily reproduce the observed light curve. The center and right panels show the largest radius companion allowable with a double-power-law fit. See Section 4 for details.

describe the data well. All these models have trouble producing a nearly linear light curve for the first 4 days and underpredict the flux around 2 days after maximum light.

## 7. X-Ray Limits on Progenitor Mass Loss

In this section, we model *Swift* X-ray observations to constrain the CSM at much larger distances and lower densities. The X-ray emission depends on both the properties of the SN, such as ejecta mass and shock velocity, and the density of the CSM, which is sculpted by the pre-SN evolution of the progenitor system. As a result, X-ray emission offers a means to probe the nature of the progenitor system that is independent of and complementary to the early light curve evolution. The environments around SN Ia progenitors are expected to be low in density ($\dot{M} \lesssim 10^{-9}$–$10^{-4} \, M_\odot \, \mathrm{yr}^{-1}$; Chomiuk et al. 2016). Under these circumstances, inverse Compton (IC) emission will dominate the X-ray emission at early times ($t \lesssim 40$ days), when the bolometric luminosity is high (Chevalier & Fransson 2006; Margutti et al. 2012).

ASASSN-18bt was observed with the *Neil Gehrels Swift Gamma-ray Burst Mission* (*Swift*; Gehrels et al. 2004) X-ray Telescope (XRT; Hill et al. 2004; Burrows et al. 2005) beginning on 2018 February 5 09:36:00 UTC (MJD = 58154.4), $\sim$10 days postexplosion. In total, 10 epochs of

observations were obtained over 40 days, covering the time period in which the supernova reached maximum light. All observations were reprocessed from level-one XRT data using the *Swift* XRTPIPELINE version 0.13.2 script, following the standard filter and screening criteria suggested in the *Swift* XRT data reduction guide[62] and the most up-to-date calibration files.

We inspected the individual observations and found no X-ray emission associated with the position of ASASSN-18bt. In order to place the strongest possible constraint on the presence of X-ray emission from this source, we combined the individual *Swift* observations for a total exposure time of 12.6 ks. We again find no evidence for X-ray emission. Due to the presence of a bright X-ray point source located at $(\alpha, \delta) = (09^h 06^m 41\overset{s}{.}6, +19°20'53'')$, $\sim$50″ away from the position of ASASSN-18bt, we used a source region centered on the position of ASASSN-18bt with a radius of 10″ combined with a standard aperture correction. We derive a $3\sigma$ count-rate upper limit of $2.9 \times 10^{-4}$ counts s$^{-1}$ in the 0.3–10.0 keV energy band. Assuming an absorbed power law with a photon index of $\Gamma = 2$ and a Galactic H I column density of $3.42 \times 10^{20}$ cm$^{-2}$ derived from Kalberla et al. (2005), we derive an unabsorbed flux limit of

---
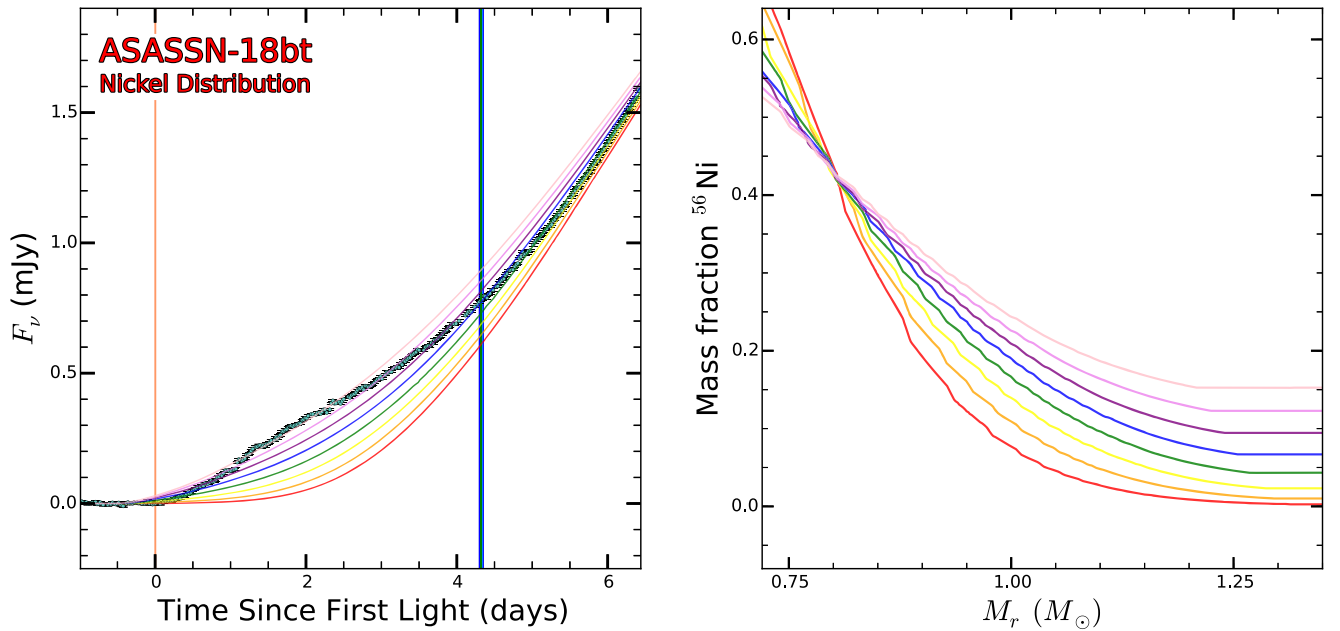
**Figure 6.** Left panel: the scaled *K2* early-time light curve of ASASSN-18bt and model light curves from Contreras et al. (2018) with variable $^{56}$Ni mixing. Model colors correspond to the $^{56}$Ni distributions shown in the right panel, which is reproduced from Contreras et al. (2018).

$1.1 \times 10^{-14}$ erg s$^{-1}$ cm$^{-2}$ or a luminosity of $L_X(0.3–10 \text{ keV}) = 3.2 \times 10^{39}$ erg s$^{-1}$.

To constrain the density of the CSM surrounding ASASSN-18bt and thus the progenitor system mass-loss rate, we follow the same procedure as described in Shappee et al. (2018) for SN 2012cg. We utilize the generalized formalism developed by Margutti et al. (2012) for IC X-ray emission from supernovae with compact progenitors. In this formalism, the IC luminosity is directly proportional to the bolometric luminosity of the supernovae. We adopt the bolometric light curve for ASASSN-18bt calculated in Li et al. (2018). The deepest limits to the density of the CSM surrounding ASASSN-18bt come from the observations at $\sim 11-14$ days postexplosion, when the bolometric luminosity was near its peak. For a constant-density CSM ($\rho_{CSM} =$ const.), we derive $\rho_{CSM} < 4.5 \times 10^5$ cm$^{-3}$ at a radius of $4 \times 10^{15}$ cm from the progenitor star. For a wind-like environment, the density of the CSM is $\rho_{CSM} = \dot{M}/(4\pi r^2 v_w)$, where $\dot{M}$ is the (constant) mass loss rate and $v_w$ is the wind velocity. Following Margutti et al. (2012), we find our observed X-ray flux limit implies a mass loss limit of $\dot{M} < 8 \times 10^{-6} M_\odot$ yr$^{-1}$ for $v_w = 100$ km s$^{-1}$, at a radius of $4.5 \times 10^{15}$ cm from the progenitor star.

In Figure 8, we compare this limit to other constraints on the density surrounding nearby SN Ia from X-ray observations (Margutti et al. 2012, 2014; Russell & Immler 2012; Shappee et al. 2014), as well as the expectations for a variety of proposed SN Ia progenitor systems. Our limit is consistent with those found by Russell & Immler (2012) for a large sample of SN Ia observed with *Swift*/XRT, but is approximately 3–4 orders of magnitude less constraining than the deep limits obtained from *Chandra* observations of the nearby SN 2011fe (Margutti et al. 2012) and SN 2014J (Margutti et al. 2014). As a result, while the *Swift*/XRT limit rules out a fraction of symbiotic progenitor systems for ASASSN-18bt, we do not expect to detect signatures from the range of main-sequence and subgiant companions allowed by the early *Kepler* light curve (Section 4).

## 8. Conclusions

ASASSN-18bt is the nearest and brightest supernova detected by *Kepler* to date, yielding a light curve with a cadence and photometric precision better than that for any other SN Ia light curve. Our fit to the very early portion of the light curve unambiguously shows a nearly linear phase, a kink, and then a steeper rise that cannot be well fit by a single-power-law model. An empirical double-power-law model fits the data reasonably well, hinting that two physical processes must be responsible for the observed rise. Thus, ASASSN-18bt joins a growing list of SNe Ia whose early light curves are not well described by a single power law, for example, SN 2012fr (Contreras et al. 2018), SN 2013dy (Zheng et al. 2013), SN 2014J (Goobar et al. 2015; Siverd et al. 2015), MUS-SES1604D (Jiang et al. 2017), iPTF16abc (Miller et al. 2018), and DLT 17u (Hosseinzadeh et al. 2017). This may be a common feature of SNe Ia that was not previously seen because high-cadence early observations of bright SNe have only become possible with the recent proliferation of high-cadence transient surveys like ASAS-SN, ATLAS, PTF, LOSS, and DLT40.

We compared the ASASSN-18bt light curves to theoretical models of three physical processes that could affect the rising light curve of a SNe Ia.

(1) We first compared the early-time light curve to the companion interaction models of Kasen (2010) for companions of various radii. We found that a single power-law rise with a companion of any radius cannot reproduce the observed *K2* light curve of ASASSN-18bt (Figure 5). We then simultaneously fit a double power law with a companion model and found nearly identically good fits for companions from 0.01 to 8 $R_\odot$ assuming a favorable viewing angle. This is because the first power law and the companion model can compensate for each other and the dark time, the power-law index, and the companion radius are degenerate. Thus, with fine-tuning, it is possible for the power law to conspire to hide the shock signature in a smooth curve. This weak constraint on the
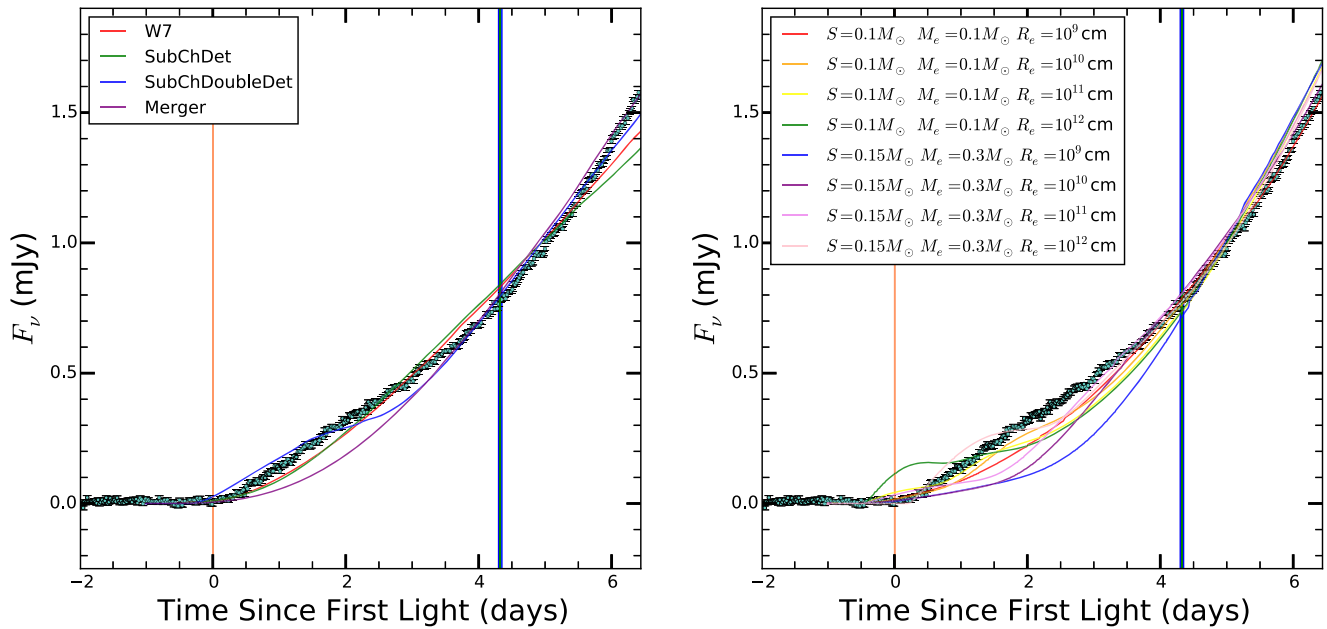
**Figure 7.** Scaled *K2* early-time light curve of ASASSN-18bt and model light curves. Left panel: synthetic light curves for a number of explosion models from Noebauer et al. (2017). Right panel: model light curves from Piro & Morozova (2016) varying the distribution of circumstellar material and $^{56}$Ni mixing.
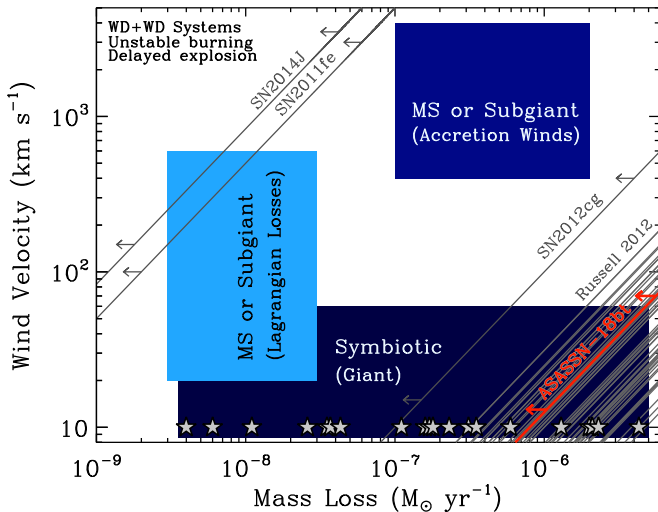


**Figure 8.** Mass loss rate vs wind velocity. Regions occupied by a variety of proposed SN Ia progenitor systems are indicated. Diagonal lines represent limits on the progenitor mass loss rates as a function of wind velocity for observed SNe Ia, obtained via X-ray observations (Margutti et al. 2012, 2014; Russell & Immler 2012; Shappee et al. 2014). For each SN, combinations of mass loss rate and wind velocity below the line are excluded. The limit for ASASSN-18bt, derived in Section 7, is plotted in red. While a fraction of observed symbiotic systems are excluded for ASASSN-18bt, a majority of proposed SN Ia progenitor systems are still allowed. For comparison, mass loss rates of Galactic symbiotic systems, for an assumed wind velocity of 10 km s$^{-1}$, are shown as gray stars (Seaquist & Taylor 1990). This figure is adapted from Margutti et al. (2014).

progenitor system demonstrates that a better, physically motivated model for the rising SN light curve is required before we can confidently and robustly use early-time light curves of SNe Ia to constrain their progenitor systems.

(2) We also compared the early light curve of ASASSN-18bt to models assuming different amounts of $^{56}$Ni mixing (Piro & Morozova 2016; Contreras et al. 2018). The amount of mixing affects the diffusion time for energy released by radioactive decay and thus the early rise of the light curve. We find that at

times less than 3 days after explosion, the light curve fits highly mixed $^{56}$Ni models, with $^{56}$Ni mass fractions of $0.15-0.2$ at approximately $0.05$ $M_\odot$ below the surface of the progenitor WD, and at later times it is more consistent with a moderately mixed model. No single, smooth $^{56}$Ni distribution accounts for the early light curve, though a nonsmooth distribution may be able to do so. We then compared ASASSN-18bt to the synthetic light curves from Noebauer et al. (2017) for a variety of explosion models. We found that only the double-detonation model, with its small amount of surface radioactive material, can qualitatively match the rise for the first few days. We note, however, that other models not tested in this work (e.g., collision models; Dong et al. 2015, 2018) may also produce similar features in the early-time light curves if they produce small amounts of shallow $^{56}$Ni.

However, the effect that $^{56}$Ni in the outer ejecta has on other observations, like the spectroscopic evolution near maximum light, must be carefully considered (e.g., Nugent et al. 1997; Kromer et al. 2010; Woosley & Kasen 2011). Perhaps the most direct observational evidence for this material is the claimed detection of the 158 keV $^{56}$Ni gamma-ray decay lines between 16 and 35 days after explosion in the nearby SN 2014J (Diehl et al. 2014; Isern et al. 2016). At these phases, the ejecta is expected to be optically thick at these wavelengths, and therefore emission from this line is expected from radioactive material located in the very outer layers. Current work in the literature suggests the measured line flux requires $\sim$0.06 (Diehl et al. 2014) to $\sim$0.03–0.08 $M_\odot$ (Isern et al. 2016) of $^{56}$Ni in the outer ejecta. Furthermore, similar to ASASSN-18bt, the rise of SN 2014J cannot be explained by a single power law (Goobar et al. 2015; Siverd et al. 2015).

(3) The interaction between supernova ejecta and the nearby CSM will also affect the early light curve of an SNe Ia. Even though nearly arbitrarily complex light curves are possible with complex distributions of nearby material, Piro & Morozova (2016) argue that nearby CSM will likely be distributed as $\rho \propto r^{-3}$. We compared the light curve of ASASSN-18bt to the theoretical light curves presented in Piro & Morozova (2016),

**Table 3**
All-sky Public Surveys

| Survey | Hemispheres | Number of sites | Depth mag | Cadence hr |
|---|---|---|---|---|
| ASAS-SN | N+S | 4 | ~18.5 | 20 |
| ATLAS | N | 2 | ~19.5 | 48 |
| ZTF | N | 1 | ~20.5 | 72 |
| Pan-STARRS | N | 1 | ~22.0 | 240 |

**Note.** Rough survey parameters for the recently expanded real-time, all-sky surveys announcing discoveries to the community. One can easily see how each survey complements the others in terms of cadence and depth. The Pan-STARRS cadence was estimated from the best case in Weryk et al. (2016).

and we find that none adequately reproduce the initial ~4 day nearly linear rise observed in ASASSN-18bt. However, more detailed theoretical studies are needed to fully explore the range of light curves that are feasible for physically motivated distributions of CSM material.

The absence of X-ray emission from ASASSN-18bt in *Swift* X-ray observations constrains the CSM at much larger distances and lower densities. For a constant-density CSM, X-ray limits constrain $\rho_{CSM} < 4.5 \times 10^5 \, cm^{-3}$ at a radius of $4 \times 10^{15} \, cm$ and a progenitor wind to have $\dot{M} < 8 \times 10^{-6} \, M_\odot \, yr^{-1}$ for $v_w = 100 \, km \, s^{-1}$, at a radius of $4.5 \times 10^{15} \, cm$ from the progenitor star. While the *Swift*/XRT limit rules out a fraction of symbiotic progenitor systems for ASASSN-18bt, the X-ray observations were not sensitive enough to detect accretion winds from main-sequence and subgiant companions.

The early-time light curves of SNe Ia may finally help resolve the uncertainty of the progenitor systems of these prolific, energetic explosive events. There is a growing class of SNe Ia with linearly rising early-time light curves for the first couple days that then steepen. The cause of this feature is still unclear. Without the well-sampled *K2* light curve presented in this work for ASASSN-18bt, the physical nature of this signature could have been confused or misinterpreted. This discovery highlights the need for more theoretical work on the expected signatures from various progenitor models. Additionally, significantly more observational work is needed to find nearby SNe Ia within about the first day of $t_1$ when interesting physical effects are not yet swamped by the $^{56}$Ni-power rising light curve. However, this work also highlights the power of well-sampled early-time data and that immediate multiband, high-cadence follow-up will be needed for progress in our understanding of SNe Ia to continue. With the recently expanded, now operational, next generation of public all-sky transient surveys, having increased cadence and sensitivity (listed in Table 3), the collection of well-sampled light curves is expected to explode. Indeed, at the writing of this manuscript, two SNe Ia have already been discovered in the TESS field of view (ASASSN-18rn and ASASSN-18tb), where studies similar to this work will be performed.

**ORCID iDs**

T. W.-S. Holoien ⑩ https://orcid.org/0000-0001-9206-3460
M. D. Stritzinger ⑩ https://orcid.org/0000-0002-5571-1833
C. S. Kochanek ⑩ https://orcid.org/0000-0001-6017-2961
E. Shaya ⑩ https://orcid.org/0000-0002-3234-8699
J. S. Brown ⑩ https://orcid.org/0000-0002-1885-6419
D. Bersier ⑩ https://orcid.org/0000-0001-7485-3020
Ping Chen ⑩ https://orcid.org/0000-0003-0853-6427
Subo Dong ⑩ https://orcid.org/0000-0002-1027-0990
J. A. Muñoz ⑩ https://orcid.org/0000-0001-9833-2959
J. L. Prieto ⑩ https://orcid.org/0000-0003-0943-0026
J. Shields ⑩ https://orcid.org/0000-0002-1560-5286
S. Villanueva, Jr. ⑩ https://orcid.org/0000-0001-6213-8804
H. Flewelling ⑩ https://orcid.org/0000-0002-1050-4056
A. N. Heinze ⑩ https://orcid.org/0000-0003-3313-4921
B. Stalder ⑩ https://orcid.org/0000-0003-0973-4900
J. L. Tonry ⑩ https://orcid.org/0000-0003-2858-9657
T. Barclay ⑩ https://orcid.org/0000-0001-7139-2724
G. Barentsen ⑩ https://orcid.org/0000-0002-3306-3484
A. M. Cody ⑩ https://orcid.org/0000-0002-3656-6706

J. Dotson ⓘ https://orcid.org/0000-0003-4206-5649
P. Garnavich ⓘ https://orcid.org/0000-0003-4069-2817
M. Gully-Santiago ⓘ https://orcid.org/0000-0002-4020-3457
C. Hedges ⓘ https://orcid.org/0000-0002-3385-8391
S. Howell ⓘ https://orcid.org/0000-0002-2532-2853
S. Margheim ⓘ https://orcid.org/0000-0001-8205-9441
R. Mushotzky ⓘ https://orcid.org/0000-0002-7962-5446
L. Migliorini ⓘ https://orcid.org/0000-0001-7386-9215
J. Bulger ⓘ https://orcid.org/0000-0003-4641-2003
E. A. Magnier ⓘ https://orcid.org/0000-0002-7965-2815
C. Z. Waters ⓘ https://orcid.org/0000-0003-1989-4879
E. Baron ⓘ https://orcid.org/0000-0001-5393-1608
Xue Li ⓘ https://orcid.org/0000-0001-8883-7179
Lingzhi Wang ⓘ https://orcid.org/0000-0002-1094-3817
Jujia Zhang ⓘ https://orcid.org/0000-0002-8296-2590
Tianmeng Zhang ⓘ https://orcid.org/0000-0002-8531-5161
P. J. Brown ⓘ https://orcid.org/0000-0001-6272-5507

## References

Alard, C. 2000, A&AS, 144, 363
Alard, C., & Lupton, R. H. 1998, ApJ, 503, 325
Antognini, J. M., Shappee, B. J., Thompson, T. A., & Amaro-Seoane, P. 2014, MNRAS, 439, 1079
Arnett, W. D. 1982, ApJ, 253, 785
Bloom, J. S., Kasen, D., Shen, K. J., et al. 2012, ApJL, 744, L17
Borucki, W. J. 2016, RPPh, 79, 036901
Brown, J. S., Stanek, K. Z., Vallely, P., et al. 2018, ATel, 11253
Brown, T. M., Baliber, N., Bianco, F. B., et al. 2013, PASP, 125, 1031
Bruzual, G., & Charlot, S. 2003, MNRAS, 344, 1000
Burrows, D. N., Hill, J. E., Nousek, J. A., et al. 2005, SSRv, 120, 165
Cardelli, J. A., Clayton, G. C., & Mathis, J. S. 1989, ApJ, 345, 245
Cartier, R., Sullivan, M., Firth, R. E., et al. 2017, MNRAS, 464, 4476
Chambers, K. C., Magnier, E. A., Metcalfe, N., et al. 2016, arXiv:1612.05560
Chevalier, R. A., & Fransson, C. 2006, ApJ, 651, 381
Chomiuk, L., Soderberg, A. M., Chevalier, R. A., et al. 2016, ApJ, 821, 119
Contreras, C., Phillips, M. M., Burns, C. R., et al. 2018, ApJ, 859, 24
Cornect, R., Brimacombe, J., Stone, G., et al. 2018, ATel, 11259
Diehl, R., Siegert, T., Hillebrandt, W., et al. 2014, Sci, 345, 1162
Dimitriadis, G., Foley, R. J., Rest, A., et al. 2018, ApJL, 870, L1
Dong, S., Katz, B., Kollmeier, J. A., et al. 2018, MNRAS, 479, L70
Dong, S., Katz, B., Kushnir, D., & Prieto, J. L. 2015, MNRAS, 454, L61
Eggleton, P. P. 1983, ApJ, 268, 368
Fang, X., Thompson, T. A., & Hirata, C. M. 2018, MNRAS, 476, 4234
Fink, M., Röpke, F. K., Hillebrandt, W., et al. 2010, A&A, 514, A53
Flewelling, H. A., Magnier, E. A., Chambers, K. C., et al. 2016, arXiv:1612.05243
Folatelli, G., Phillips, M. M., Burns, C. R., et al. 2010, AJ, 139, 120
Foley, R. J., Challis, P. J., Filippenko, A. V., et al. 2012, ApJ, 744, 38
Foreman-Mackey, D., Hogg, D. W., Lang, D., & Goodman, J. 2013, PASP, 125, 306
Garnavich, P. M., Tucker, B. E., Rest, A., et al. 2016, ApJ, 820, 23
Gehrels, N., Chincarini, G., Giommi, P., et al. 2004, ApJ, 611, 1005
Goobar, A., Kromer, M., Siverd, R., et al. 2015, ApJ, 799, 106
Hachinger, S., Mazzali, P. A., Sullivan, M., et al. 2013, MNRAS, 429, 2228
Henden, A. A., Levine, S., Terrell, D., & Welch, D. L. 2015, in AAS Meeting, 225, 336.16
Hill, J. E., Burrows, D. N., Nousek, J. A., et al. 2004, Proc. SPIE, 5165, 217
Holmbo, S., Stritzinger, M. D., Shappee, B. J., et al. 2018, arXiv:1809.01359
Hosseinzadeh, G., Sand, D. J., Valenti, S., et al. 2017, ApJL, 845, L11
Howell, S. B., Sobeck, C., Haas, M., et al. 2014, PASP, 126, 398

Hoyle, F., & Fowler, W. A. 1960, ApJ, 132, 565
Iben, I., Jr., & Tutukov, A. V. 1984, ApJS, 54, 335
Im, M., Choi, C., Yoon, S.-C., et al. 2015, ApJS, 221, 22
Isern, J., Jean, P., Bravo, E., et al. 2016, A&A, 588, A67
Jiang, J.-A., Doi, M., Maeda, K., et al. 2017, Natur, 550, 80
Kalberla, P. M. W., Burton, W. B., Hartmann, D., et al. 2005, A&A, 440, 775
Kasen, D. 2010, ApJ, 708, 1025
Kasen, D., Röpke, F. K., & Woosley, S. E. 2009, Natur, 460, 869
Katz, B., & Dong, S. 2012, arXiv:astro-ph/1211.4584
Koch, D. G., Borucki, W. J., Basri, G., et al. 2010, ApJL, 713, L79
Kriek, M., van Dokkum, P. G., Labbé, I., et al. 2009, ApJ, 700, 221
Kromer, M., Sim, S. A., Fink, M., et al. 2010, ApJ, 719, 1067
Leadbeater, R. 2018, Transient Name Server Classification Report 159
Li, W., Wang, X., Vinko, J., et al. 2018, ApJ, 870, 12
Liu, Z. W., Pakmor, R., Röpke, F. K., et al. 2012, A&A, 548, A2
Magnier, E. A., Schlafly, E. F., Finkbeiner, D. P., et al. 2016, arXiv:1612.05242
Margutti, R., Parrent, J., Kamble, A., et al. 2014, ApJ, 790, 52
Margutti, R., Soderberg, A. M., Chomiuk, L., et al. 2012, ApJ, 751, 134
Marietta, E., Burrows, A., & Fryxell, B. 2000, ApJS, 128, 615
Marion, G. H., Brown, P. J., Vinko, J., et al. 2016, ApJ, 820, 92
Miller, A. A., Cao, Y., Piro, A. L., et al. 2018, ApJ, 852, 100
Morozova, V., Piro, A. L., Renzo, M., et al. 2015, ApJ, 814, 63
Noebauer, U. M., Kromer, M., Taubenberger, S., et al. 2017, MNRAS, 472, 2787
Nomoto, K. 1982, ApJ, 253, 798
Nomoto, K., Thielemann, F.-K., & Yokoi, K. 1984, ApJ, 286, 644
Nugent, P., Baron, E., Branch, D., Fisher, A., & Hauschildt, P. H. 1997, ApJ, 485, 812
Nugent, P. E., Sullivan, M., Cenko, S. B., et al. 2011, Natur, 480, 344
Olling, R. P., Mushotzky, R., Shaya, E. J., et al. 2015, Natur, 521, 332
Pakmor, R., Kromer, M., Taubenberger, S., et al. 2012, ApJL, 747, L10
Pan, K.-C., Ricker, P. M., & Taam, R. E. 2012a, ApJ, 760, 21
Pan, K.-C., Ricker, P. M., & Taam, R. E. 2012b, ApJ, 750, 151
Pejcha, O., Antognini, J. M., Shappee, B. J., & Thompson, T. A. 2013, MNRAS, 435, 943
Piro, A. L., & Morozova, V. S. 2016, ApJ, 826, 96
Piro, A. L., & Nakar, E. 2013, ApJ, 769, 67
Piro, A. L., & Nakar, E. 2014, ApJ, 784, 85
Podsiadlowski, P. 2003, arXiv:astro-ph/0303660
Russell, B. R., & Immler, S. 2012, ApJL, 748, L29
Schlafly, E. F., & Finkbeiner, D. P. 2011, ApJ, 737, 103
Schneider, S. E., Thuan, T. X., Magri, C., & Wadiak, J. E. 1990, ApJS, 72, 245
Schwab, J., Shen, K. J., Quataert, E., Dan, M., & Rosswog, S. 2012, MNRAS, 427, 190
Seaquist, E. R., & Taylor, A. R. 1990, ApJ, 349, 313
Shappee, B. J., Kochanek, C. S., & Stanek, K. Z. 2013, ApJL, 765, 150
Shappee, B. J., Piro, A. L., Holoien, T. W.-S., et al. 2016, ApJ, 826, 144
Shappee, B. J., Piro, A. L., Stanek, K. Z., et al. 2018, ApJ, 855, 6
Shappee, B. J., Prieto, J. L., Grupe, D., et al. 2014, ApJ, 788, 48
Shappee, B. J., & Thompson, T. A. 2013, ApJ, 766, 64
Shen, K. J., Bildsten, L., Kasen, D., & Quataert, E. 2012, ApJ, 748, 35
Silverman, J. M., Ganeshalingam, M., Cenko, S. B., et al. 2012, ApJL, 756, L7
Sim, S. A., Proga, D., Miller, L., Long, K. S., & Turner, T. J. 2010, MNRAS, 408, 1396
Siverd, R. J., Goobar, A., Stassun, K. G., & Pepper, J. 2015, ApJ, 799, 105
Stritzinger, M. D., Shappee, B. J., Piro, A. L., et al. 2018, ApJL, 864, L35
Thompson, T. A. 2011, ApJ, 741, 82
Tonry, J. L., Denneau, L., Heinze, A. N., et al. 2018, PASP, 130, 064505
Tutukov, A. V., & Yungelson, L. R. 1979, Acta Astron., 29, 665
Webbink, R. F. 1984, ApJ, 277, 355
Weryk, R. J., Lily, E., Chastel, S., et al. 2016, arXiv:1607.04895
Wheeler, J. C., Lecar, M., & McKee, C. F. 1975, ApJ, 200, 145
Whelan, J., & Iben, I., Jr. 1973, ApJ, 186, 1007
Woosley, S. E., & Kasen, D. 2011, ApJ, 734, 38
Zheng, W., Silverman, J. M., Filippenko, A. V., et al. 2013, ApJL, 778, L15